10. O. V. Mikhnenko *et al.*, *Energy Environ. Sci.* **5**, 6960 (2012).
11. J. J. M. Halls *et al.*, *Nature* **376**, 498–500 (1995).
12. M. M. Lee, J. Teuscher, T. Miyasaka, T. N. Murakami, H. J. Snaith, *Science* **338**, 643–647 (2012).
13. H.-S. Kim *et al.*, *Sci. Rep.* **2**, 591 (2012).
14. J. H. Heo *et al.*, *Nat. Photonics* **7**, 486 (2013).
15. J. H. Noh, S. H. Im, J. H. Heo, T. N. Mandal, S. I. Seok, *Nano Lett.* **13**, 1764–1769 (2013).
16. J. M. Ball, M. M. Lee, A. Hey, H. J. Snaith, *Energy Environ. Sci.* **6**, 1739 (2013).
17. J. Burschka *et al.*, *Nature* **499**, 316–319 (2013).
18. A. Abrusci *et al.*, *Nano Lett.* **13**, 3124–3128 (2013).
19. M. Liu, M. B. Johnston, H. J. Snaith, *Nature* **501**, 395–398 (2013).
20. W. Zhang *et al.*, *Nano Lett.* **13**, 4505–4510 (2013).
21. A. Kojima, K. Teshima, Y. Shirai, T. Miyasaka, *J. Am. Chem. Soc.* **131**, 6050–6051 (2009).
22. P. E. Shaw, A. Ruseckas, I. D. W. Samuel, *Adv. Mater.* **20**, 3516–3520 (2008).
23. T. Ishihara, *J. Lumin.* **60-61**, 269–274 (1994).
24. K. Tanaka *et al.*, *Solid State Commun.* **127**, 619–623 (2003).
25. M. Hirasawa, T. Ishihara, T. Goto, K. Uchida, N. Miura, *Physica B* **201**, 427–430 (1994).
26. G. E. Eperon, V. M. Burlakov, P. Docampo, A. Goriely, H. J. Snaith, *Advanced Funtional Materials*, published online 9 September 2013 (10.1002/adfm.201302090).
27. J. R. Lakowicz, *Principles of Fluorescence Spectroscopy* (Springer London, Limited, 2007).

Acknowledgments: This project was funded by the Engineering and Physical Sciences Research Council, the European Research Council (ERC-StG 2011 HYPER project 279881), Oxford Photovoltaics through a Nanotechnology KTN CASE award, and by a Royal Society Wolfson exchange grant. The authors thank V. D'Innocenzo for technical support and J. Alexander-Webber for atomic force microscopy supporting measurements. A.P. and H.J.S. thank "The Royal Society International Exchanges Scheme 2012/R2." S.D.S. thanks Worcester College, Oxford, for additional financial support. Solar cells based on the perovskite materials studied in this report are being commercialized by Oxford Photovoltaics, a spin-out company from the University of Oxford.

Supplementary Materials
www.sciencemag.org/content/342/6156/341/suppl/DC1
Materials and Methods
Figs. S1 to S4
Tables S1 to S3

30 July 2013; accepted 4 September 2013
10.1126/science.1243982

Long-Range Balanced Electron- and Hole-Transport Lengths in Organic-Inorganic $CH_3NH_3PbI_3$

Guichuan Xing,[1]* Nripan Mathews,[2,3,4]*† Shuangyong Sun,[2] Swee Sien Lim,[1] Yeng Ming Lam,[2,5] Michael Grätzel,[3,6] Subodh Mhaisalkar,[2,3] Tze Chien Sum[1]†

Low-temperature solution-processed photovoltaics suffer from low efficiencies because of poor exciton or electron-hole diffusion lengths (typically about 10 nanometers). Recent reports of highly efficient $CH_3NH_3PbI_3$-based solar cells in a broad range of configurations raise a compelling case for understanding the fundamental photophysical mechanisms in these materials. By applying femtosecond transient optical spectroscopy to bilayers that interface this perovskite with either selective-electron or selective-hole extraction materials, we have uncovered concrete evidence of balanced long-range electron-hole diffusion lengths of at least 100 nanometers in solution-processed $CH_3NH_3PbI_3$. The high photoconversion efficiencies of these systems stem from the comparable optical absorption length and charge-carrier diffusion lengths, transcending the traditional constraints of solution-processed semiconductors.

An ideal solar cell material should combine good optical absorption characteristics with efficient charge-transport properties. Low-temperature solution-processed light-harvesting films prepared by techniques such as spin-coating and chemical bath deposition are typically amorphous or poorly crystalline (*1*–*3*), consequently suffering from poor charge-carrier transport (*4*). This limitation necessitates device designs that decouple light absorption and charge-carrier transport lengths, including light-trapping strategies such as plasmonics (*5*, *6*) as well as the sensitized solar cell architecture (*7*, *8*). The recent development of organic-inorganic halide perovskite materials such as $CH_3NH_3PbI_3$ as light harvesters in solid-state sensitized solar cells has led to reports of impressive efficiency values of up to 15% (*9*). This remarkable material has been used in a variety of photovoltaic architectures. A configuration used by Kim *et al.* (*10*) and Heo *et al.* (*11*) sandwiches the thin perovskite layer between a rough mesoporous TiO_2 photoanode and a hole-transporting layer such as 2,2′,7,7′-tetrakis(*N*,*N*-di-*p*-methoxyphenylamino)-9,9′-spirobifluorene (Spiro-OMeTAD). Lee *et al.* (*12*) have shown that efficient solar cells can be fabricated by replacing the TiO_2 photoanode with an insulating Al_2O_3 scaffold, implying good electron-transport properties. Unexpectedly, Etgar *et al.* (*13*) reported an efficiency of 5.5% in a configuration without the hole-transporting layer, indicating good hole-transport properties. These indications of ambipolar charge-transport capabilities are supported by a recent report by Ball *et al.* (*14*) that demonstrated that ~350-nm-thick planar films sandwiched between a TiO_2 compact layer and a hole-transporting layer can generate short-circuit current densities of 15 mA/cm^2. These reports together imply that the electron- and hole-transport lengths within these organic-inorganic hybrid materials are high. Nonetheless, the innate dynamics of the photoexcited electrons and holes in $CH_3NH_3PbI_3$ driving the high efficiencies in these solar cells are unknown. Herein, through femtosecond transient optical spectroscopy of $CH_3NH_3PbI_3$ heterojunctions with selective electron and hole extraction, we successfully decoupled electron and hole dynamics and show evidence of long electron- and hole-transport lengths (both over 100 nm). Our findings indicate that this class of materials does not suffer from the bottleneck of low collection lengths that handicap typical low-temperature solution-processed photovoltaic materials.

In this study, electron-extraction layers {such as [6,6]-phenyl-C_{61}-butyric acid methyl ester (PCBM), C_{60}} with conduction band levels below that of $CH_3NH_3PbI_3$ and hole-extraction layers [such as Spiro-OMeTAD, poly(3,4-ethylenedioxythiophene) poly(styrenesulfonate) (PEDOT:PSS)] with valence band levels above $CH_3NH_3PbI_3$ were interfaced to $CH_3NH_3PbI_3$ to permit decoupling of the electron and hole dynamics (fig. S1). Comparing measurements on bare $CH_3NH_3PbI_3$ against $CH_3NH_3PbI_3$/hole acceptor bilayers and $CH_3NH_3PbI_3$/electron acceptor bilayers enables identification of electron and hole signatures in the organic-inorganic halide. Under identical experimental conditions, the photoluminescence (PL) quantum yield of the 65-nm-thick $CH_3NH_3PbI_3$ is greatly reduced when the perovskite is interfaced with an electron-extracting PCBM layer or a hole-extracting Spiro-OMeTAD layer (Fig. 1A). The PL intensity is quenched by a factor of 12.5 in the bilayer with Spiro-OMeTAD and by a factor of 50 in the bilayer with PCBM (table S1). Given that the current configurations are ideal layered systems (figs. S2 and S3), these high degrees of PL quenching, comparable to closely blended donor-acceptor system, are particularly revealing (*15*–*19*). With a linear absorption coefficient of 5.7×10^4 cm^{-1} at 600 nm (Fig. 2A and fig. S4), near-homogenous generation of the charge carriers in these 65-nm $CH_3NH_3PbI_3$ layers can be ensured (*20*). The PL quenching is expected to originate from the charge-carrier extraction across the interface (*21*–*27*). Efficient PL quenching suggests that the charge-carrier diffusion length inside the $CH_3NH_3PbI_3$

[1]Division of Physics and Applied Physics, School of Physical and Mathematical Sciences, Nanyang Technological University (NTU), 21 Nanyang Link, 637371 Singapore. [2]School of Materials Science and Engineering, NTU, Nanyang Avenue, 639798 Singapore. [3]Energy Research Institute @NTU (ERI@N), Research Techno Plaza, X-Frontier Block, Level 5, 50 Nanyang Drive, 637553 Singapore. [4]Singapore-Berkeley Research Initiative for Sustainable Energy, 1 Create Way, 138602 Singapore. [5]Institute of Materials for Electronic Engineering II, Rheinisch Westfälische Technische Hochschule–Aachen, Sommerfeldstrasse 24, D-52074 Aachen, Germany. [6]Laboratory of Photonics and Interfaces, Department of Chemistry and Chemical Engineering, Swiss Federal Institute of Technology, Station 6, CH-1015 Lausanne, Switzerland.

*These authors contributed equally to this work.
†Corresponding author. E-mail: tzechien@ntu.edu.sg (T.C.S.); nripan@ntu.edu.sg (N.M.)

layer is comparable to or longer than the layer thickness (65 nm). Correspondingly, the PL lifetimes were also substantially shortened when $CH_3NH_3PbI_3$ was interfaced with the PCBM or Spiro-OMeTAD layer (Fig. 1B), with fitted lifetimes and SEMs of 4.5 ± 0.3, 0.37 ± 0.02, and 0.64 ± 0.03 ns for $CH_3NH_3PbI_3$, $CH_3NH_3PbI_3$/PCBM, and $CH_3NH_3PbI_3$/Spiro-OMeTAD, respectively.

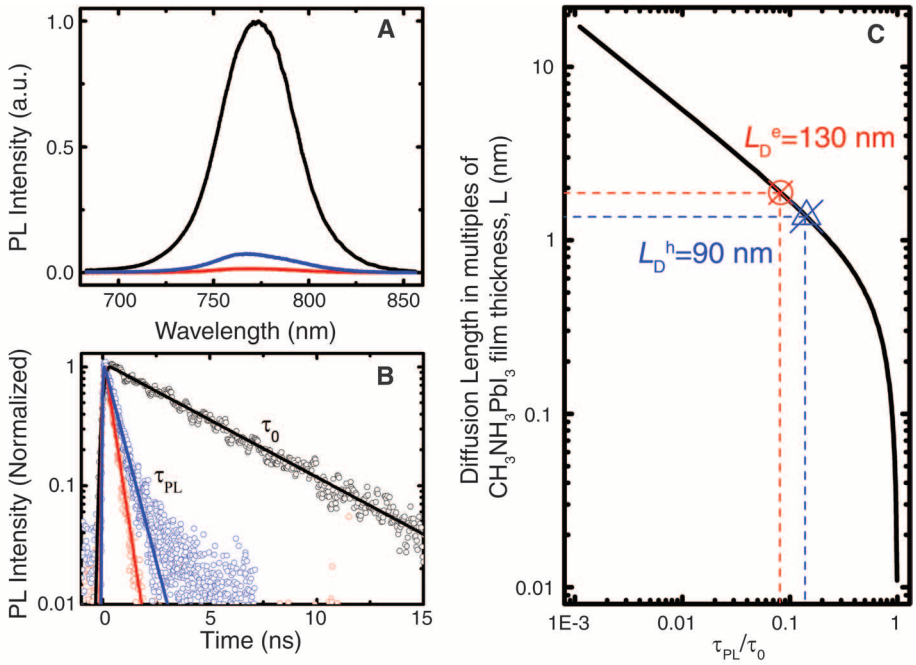

Fig. 1. Photoluminescence spectroscopy. (**A**) Time-integrated PL spectra and (**B**) Time-resolved PL decay transients measured at 760 ± 10 nm for quartz/$CH_3NH_3PbI_3$(65 nm) (black), quartz/$CH_3NH_3PbI_3$ (65 nm)/PCBM (red), quartz/$CH_3NH_3PbI_3$(65 nm)/Spiro-OMeTAD (blue) films in vacuum after excitation at 600 nm (1 KHz, 150 fs, 1.3 μJ/cm^2). The solid lines in (B) are the single-exponential fits of the PL decay transients. a.u., arbitrary units. (**C**) A plot of exciton diffusion length versus PL lifetime quenching ratios based on Eq. S5. Diffusion length is scaled in multiples of $CH_3NH_3PbI_3$ layer thickness (L = 65 nm).

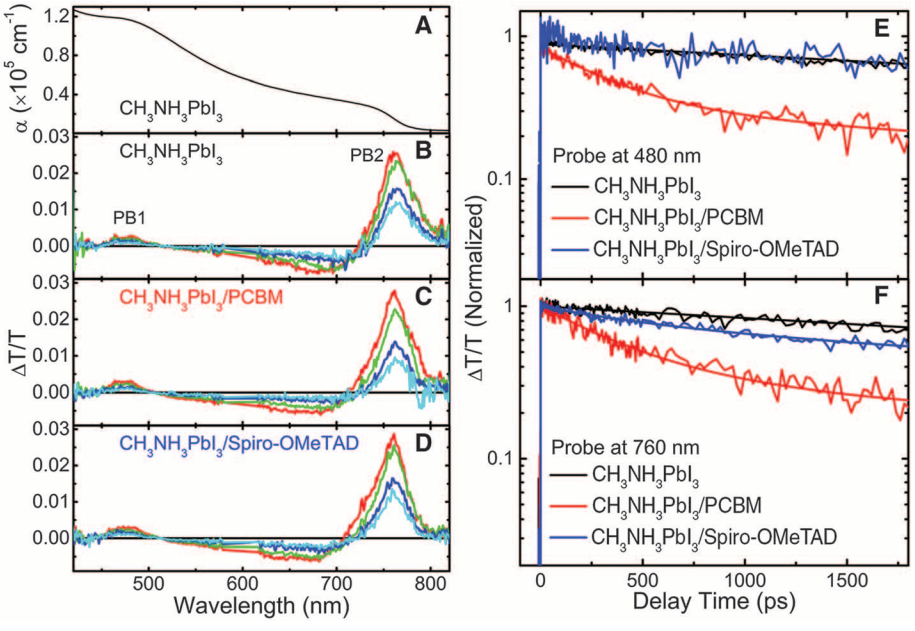

Fig. 2. Steady-state and transient absorption spectroscopy. (**A**) UV-visible absorbance spectrum for a pure $CH_3NH_3PbI_3$ layer. (**B** to **D**) Differential transmission ($\Delta T/T$) spectra for $CH_3NH_3PbI_3$, $CH_3NH_3PbI_3$/PCBM, and $CH_3NH_3PbI_3$/Spiro-OMeTAD films in vacuum after excitation at 600 nm (1 KHz, 150 fs, 13 μJ/cm^2): red (1 ps), green (100 ps), blue (500 ps), and cyan (1 ns). Normalized bleaching kinetics at (**E**) 480 and (**F**) 760 nm for the films in vacuum after excitation at 600 nm (1 KHz, 150 fs, 1.3 μJ/cm^2).

The single exponential PL decay indicates the good crystalline quality of the samples. By using the relation ($1/\tau_{Heterojunction} = 1/\tau_{Perovskite} + 1/\tau_{CT}$), the charge-carrier transfer time, τ_{CT}, and efficiency can be estimated to be 0.40 ns and 92%, respectively, for $CH_3NH_3PbI_3$/PCBM and 0.75 ns and 86% for $CH_3NH_3PbI_3$/Spiro-OMeTAD. The slight variation between the charge carrier transfer efficiencies obtained by using steady-state PL (Fig. 1A and table S1) and transient PL can be attributed to (i) extremely fast charge-carrier transfer at the interface (that cannot be monitored at the current temporal resolution) and (ii) the dependence of the steady-state PL on the light reflection, scattering, and refraction by the additional PCBM and Spiro-OMeTAD layers in the heterojunctions. Next, a charge-carrier extraction model based on diffusion was used to estimate the charge carrier diffusion lengths (see supplementary materials). Figure 1C shows the dependence of the charge-carrier diffusion length on the PL lifetime quenching ratios obtained from the analytical solution of the model. By assuming that charge-carrier quenching occurs only at the extraction layer interface with 100% efficiency, we obtained minimum estimates of the extracted electron and hole diffusion lengths of 130 and 90 nm. By comparison, solution-processed organic conjugated materials have typical diffusion lengths of about 10 nm (*21*–*23*), thermally deposited organic molecules have typical diffusion lengths of 10 to 50 nm (*24*–*26*), and colloidal quantum dot films have diffusion lengths of ~30 nm (organic cross-linked) and ~80 nm (hybrid surface passivated) (*27*). Thus, the conservatively estimated long diffusion lengths in the low-temperature solution-processed $CH_3NH_3PbI_3$ films compare favorably.

To improve the accuracy of these estimated values from the direct PL approach and to obtain more details on the photoexcited charge carrier dynamics, we also performed complementary transient absorption spectroscopy (TAS) measurements (*10*, *17*, *28*–*33*). Due to the large absorption coefficients and the long charge-carrier diffusion lengths, low pump fluence is essential to avoid extensive Auger recombination in $CH_3NH_3PbI_3$ (figs. S6 to S9). Figure 2A shows the linear absorption spectrum of $CH_3NH_3PbI_3$ spanning the ultraviolet (UV) to near infrared (800 nm) with two distinct peaks located at 480 and 760 nm, in agreement with earlier publications (*9*–*14*, *20*). The second absorption peak (760 nm) is attributed to the direct gap transition from the first valence band maximum (VB1) to the conduction band minimum (CB1). However, the origin of the first absorption peak (480 nm) is still unresolved. Representative TA spectra of $CH_3NH_3PbI_3$ and its bilayer counterparts over the same spectral region are shown in Fig. 2, B to D, with two pronounced photobleaching (PB) bands. These long-lived PB peaks are located at almost the same spectral positions as the two absorption peaks. The bleaches at 480 and 760 nm are labeled as PB1 and PB2, respectively, and are attributed to

state-filling (*34*). For 600-nm photoexcitation, it is reasonable to attribute the 760-nm PB2 band to state-filling effects (which include the hole population of VB1, the electron population of CB1, and the interband stimulated emission) (*10*, *17*, *28*–*33*). However, it is not straightforward to assign the transitions associated with the 480-nm PB1 band. Given that the photoexcitation energy (of ~ 2.06 eV for 600-nm wavelength) is smaller than the energy of the PB1 peak (2.58 eV), only one of the two energy states involving this PB transition could be populated. The long-lived nature of this PB band further suggests that the populated energy level should be either VB1 or CB1 (see supplementary materials for a more detailed discussion of the assignment).

Upon selective excitation of the $CH_3NH_3PbI_3$ layer, no new PB or photoinduced absorption bands are observed when the electron or hole extraction layer is present. A comparative study at the respective probe wavelengths of PB1 and PB2 would thus yield detailed information about the charge-carrier dynamics. For pure $CH_3NH_3PbI_3$, the recombination dynamics at different probe wavelengths are relatively invariant over a range of pump fluences where second order effects are insignificant (fig. S6). All these decay transients are well fitted with a single exponential time constant of 5.6 ± 0.1 ns, which is longer than the measured PL lifetime of 4.5 ± 0.3 ns (table S1). Because time-resolved PL cannot monitor the recombination dynamics of all the photoexcited carriers, this finding suggests that the PL lifetime in pure $CH_3NH_3PbI_3$ is limited by the minority carrier lifetime. Correlating these PL lifetimes with the TA lifetimes of the bilayers allows us to identify the minority charge carriers.

With the PCBM (electron acceptor) layer present, both PB1 and PB2 bleaching peaks show an additional fast lifetime component of 0.37 ± 0.02 ns (Fig. 2, E and F), which is closely matched to the measured PL lifetime. This suggests that electrons are the minority charge carriers in $CH_3NH_3PbI_3$. Because PB1 and PB2 dynamics are simultaneously affected by the electron extraction layer, the probes monitor the electron population in the CB1. For the $CH_3NH_3PbI_3$/Spiro-OMeTAD (hole acceptor) samples, only PB2 exhibits an additional fast decay lifetime of 0.59 ± 0.03 ns (Fig. 2E), which is slightly faster than the PL lifetime of 0.64 ± 0.03 ns (table S1). This indicates that PB2 also reflects the hole population of VB1 (i.e., the transitions between VB1 and CB1). PB1 on the other hand is only related to the electron population in CB1 [i.e., the transitions between the lower valence band (VB2) and CB1] (Fig. 3C). By comparing the PB1 decays between pure $CH_3NH_3PbI_3$ and $CH_3NH_3PbI_3$/PCBM, we determined the electron extraction time and efficiency in $CH_3NH_3PbI_3$/PCBM to be 0.40 ± 0.05 ns and 68%, respectively. Figure 2E also shows that about 27% of the photogenerated electrons are possibly trapped and therefore contribute neither to the electron extraction from $CH_3NH_3PbI_3$ to PCBM nor to the radiative recombination. By comparing the decay at PB2 between pure $CH_3NH_3PbI_3$ and $CH_3NH_3PbI_3$/Spiro-OMeTAD, we estimate the hole extraction time in $CH_3NH_3PbI_3$/Spiro-OMeTAD to be 0.66 ± 0.05 ns. However, given that the TA signal at PB2 is a combination of signals from both electrons and holes, it is difficult to estimate the detailed hole-extraction efficiency at this stage.

The origins of PB1 and PB2 suggest the possibility of hot holes cooling from VB2 to VB1 after excitation of $CH_3NH_3PbI_3$ across the VB2-CB1 gap. Such hot-hole cooling dynamics could be validated through varying the pump wavelengths. After 3.10-eV (400-nm) excitation, Fig. 3A shows a very fast bleach buildup for PB1, which is close to the 150-fs laser pulse duration. Subsequently, hole localization from VB2 to VB1 occurs (within ~0.4 ps). The decay of the PB1 transient (indicative of the depopulation of VB2) is well matched with a concomitant rise of the bleach signal at PB2 (indicative of VB1 being populated), both at 0.4 ± 0.1 ps. On the other hand, excitations with lower energy photons [e.g., across the VB1-CB1 gap using 2.07-eV (600-nm) pulses] do not excite carriers in VB2, and therefore such hot-hole cooling dynamics are absent (Fig. 3B). This 0.4-ps hot-hole cooling is much slower than that in most organic semiconductors (~100 fs) (*30*, *35*). Potentially, these hot-hole energies could be efficiently extracted before the hot holes cool down to VB1 through optimizing the device configuration.

From fitting the TA decay dynamics with the diffusion model, we found the electron and hole diffusion coefficients to be 0.036 and 0.022 cm^2/s, respectively. By using these values, we calculated the electron and hole diffusion lengths (L_D) perpendicular to the film surface to be $L_D^e = 130$ nm and $L_D^h = 110$ nm, where $L_D = \sqrt{D\tau_{TA}}$. As expected, the L_D^h (majority carrier diffusion length) determined here is longer than that extracted from the more-direct PL approach presented earlier, which is sensitive to the minority carrier dynamics. The long transport lengths associated with $CH_3NH_3PbI_3$ are linked to its crystal structure, which consists of corner-connected PbI_6 octahedra that form a three-dimensional framework (*36*). Other organic-inorganic halide materials based on Sn have also displayed good charge-transport properties (*37*, *38*). The slightly shorter diffusion length of the holes compared with the electrons is consistent with the hole's larger effective mass and larger positive space charge-limited transport. Nonetheless, these values are relatively balanced compared with typical values reported in bulk heterojunction solar cells, where the electron- and hole-transport lengths (proportional to their mobility) differ by orders of magnitude, resulting in space charge-limited photocurrents (*39*). These balanced long charge-carrier diffusion lengths would account for the remarkable performances reported for these $CH_3NH_3PbI_3$ devices. These L_D values are underestimated mainly because of the assumption that no quenching at the $CH_3NH_3PbI_3$-quartz or -vacuum interfaces occur. The measured carrier lifetimes, τ_0, are more susceptible to the nonideality of these interfaces in these thinner spin-coated $CH_3NH_3PbI_3$ layers, leading to smaller τ_0 and consequently shorter L_D. Measurements in more "bulk-like" samples would yield longer

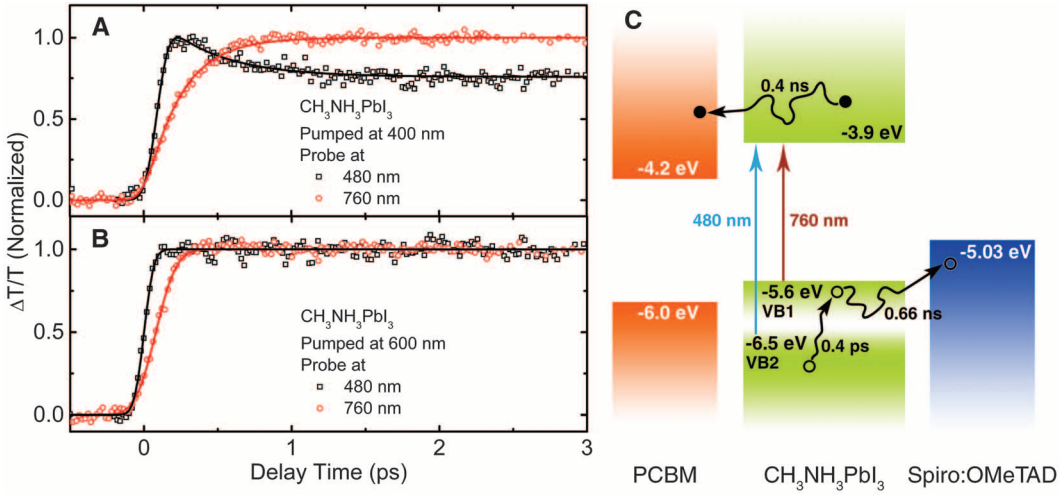

Fig. 3. Early time dynamics. Normalized bleaching kinetics at 480 and 760 nm in a short time range show the intervalence band hot-hole cooling for $CH_3NH_3PbI_3$ film (in vacuum) after excitation at (**A**) 400 nm (1 μJ/cm^2) and (**B**) 600 nm (1.3 μJ/cm^2). (**C**) A schematic illustrating the hot-hole cooling and charge recombination within $CH_3NH_3PbI_3$ and charge separation at the $CH_3NH_3PbI_3$/PCBM and $CH_3NH_3PbI_3$/Spiro-OMeTAD interfaces. The approximate positions of VB1 and VB2 were obtained from the TA measurements.

τ_0 and higher L_D (submicrometer) (Fig. 1C). From the linear absorption coefficients (Fig. 2A), the absorption lengths are $L_\alpha \sim 100$ nm (at $\lambda = 500$ nm). These conservatively estimated carrier diffusion lengths measured in $CH_3NH_3PbI_3$ are comparable to the optical absorption lengths for $\lambda \leq 500$ nm but are shorter than the absorption lengths at longer wavelengths. Increasing the optical thickness of these layers through light-trapping architectures compensates for this slight mismatch, accounting for the high photoconversion efficiencies reported in these systems (*9*–*14*, *40*).

References and Notes

1. P. M. Beaujuge, J. M. J. Fréchet, *J. Am. Chem. Soc.* **133**, 20009–20029 (2011).
2. A. Facchetti, *Chem. Mater.* **23**, 733–758 (2011).
3. R. S. Selinsky, Q. Ding, M. S. Faber, J. C. Wright, S. Jin, *Chem. Soc. Rev.* **42**, 2963–2985 (2013).
4. H. Sirringhaus, *Adv. Mater.* **17**, 2411–2425 (2005).
5. H. A. Atwater, A. Polman, *Nat. Mater.* **9**, 205–213 (2010).
6. B. Wu *et al.*, *Nat. Commun.* **4**, 2004 (2013).
7. B. O'Regan, M. Grätzel, *Nature* **353**, 737–740 (1991).
8. A. Yella *et al.*, *Science* **334**, 629–634 (2011).
9. J. Burschka *et al.*, *Nature* **499**, 316–319 (2013).
10. H. S. Kim *et al.*, *Sci. Rep.* **2**, 591 (2012).
11. J. H. Heo *et al.*, *Nat. Photonics* **7**, 486–491 (2013).
12. M. M. Lee, J. Teuscher, T. Miyasaka, T. N. Murakami, H. J. Snaith, *Science* **338**, 643–647 (2012); 10.1126/science.1228604.
13. L. Etgar *et al.*, *J. Am. Chem. Soc.* **134**, 17396–17399 (2012).
14. J. M. Ball, M. M. Lee, A. Hey, H. J. Snaith, *Energy Environ. Sci.* **6**, 1739 (2013).
15. W. J. E. Beek, M. M. Wienk, R. A. J. Janssen, *Adv. Funct. Mater.* **16**, 1112–1116 (2006).
16. J. K. J. van Duren *et al.*, *Adv. Funct. Mater.* **14**, 425–434 (2004).
17. J. Piris *et al.*, *J. Phys. Chem. C* **113**, 14500–14506 (2009).
18. Y. Kim *et al.*, *J. Mater. Sci.* **40**, 1371–1376 (2005).
19. Y. Kim *et al.*, *J. Phys. Chem. C* **111**, 8137–8141 (2007).
20. J. H. Im, C. R. Lee, J. W. Lee, S. W. Park, N. G. Park, *Nanoscale* **3**, 4088–4093 (2011).
21. P. E. Shaw, A. Ruseckas, I. D. W. Samuel, *Adv. Mater.* **20**, 3516–3520 (2008).
22. A. Haugeneder *et al.*, *Phys. Rev. B* **59**, 15346–15351 (1999).
23. J. E. Kroeze, T. J. Savenije, M. J. W. Vermeulen, J. M. Warman, *J. Phys. Chem. B* **107**, 7696–7705 (2003).
24. R. R. Lunt, J. B. Benziger, S. R. Forrest, *Adv. Mater.* **22**, 1233–1236 (2010).
25. H. Najafov, B. Lee, Q. Zhou, L. C. Feldman, V. Podzorov, *Nat. Mater.* **9**, 938–943 (2010).
26. P. Peumans, A. Yakimov, S. R. Forrest, *J. Appl. Phys.* **93**, 3693 (2003).
27. D. Zhitomirsky, O. Voznyy, S. Hoogland, E. H. Sargent, *ACS Nano* **7**, 5282–5290 (2013).
28. V. I. Klimov, *Annu. Rev. Phys. Chem.* **58**, 635–673 (2007).
29. G. N. Ostojic *et al.*, *Phys. Rev. Lett.* **94**, 097401 (2005).
30. G. Grancini *et al.*, *Nat. Mater.* **12**, 29–33 (2013).
31. G. Grancini *et al.*, *J. Phys. Chem. Lett.* **3**, 517–523 (2012).
32. A. A. Bakulin, J. C. Hummelen, M. S. Pshenichnikov, P. H. M. Van Loosdrecht, *Adv. Funct. Mater.* **20**, 1653–1660 (2010).
33. M. L. Mueller, X. Yan, B. Dragnea, L. S. Li, *Nano Lett.* **11**, 56–60 (2011).
34. Typically, PB peaks in TAS can arise from Coulomb interaction or state filling of the quasi-particles. In the former case, coulombic interaction among the excitons gives rise to a shift in energy of the probe beam–induced transitions, which occur in the vicinity of the excitons generated by the earlier pump beam. Such a phenomenon is commonly observed in quantum-confined low-dimensional systems or under high fluence excitation. In this mechanism, the occurrence of the PB peaks usually coincides with the occurrence of adjacent photoinduced absorption peaks because of the shift or broadening of the absorption peak. Furthermore, the PB peak positions will also shift with increasing pump fluence. The absence of photoinduced absorption peaks or pump fluence dependence of the PB peaks in these $CH_3NH_3PbI_3$ films allows us to rule out Coulomb interaction. On the other hand, state filling arises because of the changes in population of the various electronic states brought about by the initial pump beam. Hence, it will only influence probe beam–induced transitions that involve electronic states with changed populations.
35. A. E. Jailaubekov *et al.*, *Nat. Mater.* **12**, 66–73 (2013).
36. T. Baikie *et al.*, *J. Mater. Chem. A* **1**, 5628 (2013).
37. C. R. Kagan, D. B. Mitzi, C. D. Dimitrakopoulos, *Science* **286**, 945–947 (1999).
38. D. B. Mitzi, S. Wang, C. A. Feild, C. A. Chess, A. M. Guloy, *Science* **267**, 1473–1476 (1995).
39. P. W. M. Blom, V. D. Mihailetchi, L. J. A. Koster, D. E. Markov, *Adv. Mater.* **19**, 1551–1566 (2007).
40. W. Zhang *et al.*, *Nano Lett.* **13**, 4505–4510 (2013).

Acknowledgments: The authors thank M. Duchamp and C. Boothroyd from Ernst Ruska-Centrum, Forschungszentrum Jülich, Germany, for the FIB and transmission electron microscopy work carried out. Financial support from NTU startup grant M4080514, School of Physical and Mathematical Sciences collaborative research award M4080536, Singapore National Research Foundation through the Competitive Research Program (NRF-CRP4-2008-03), and the Singapore-Berkeley Research Initiative for Sustainable Energy (SinBeRISE) program is gratefully acknowledged. M.G. thanks the European Research Council for financial support under the Advanced Research Grant (ARG 247404) "Mesolight."

Supplementary Materials

www.sciencemag.org/content/342/6156/344/suppl/DC1
Materials and Methods
Fig. S1 to S9
Table S1
References (*41*, *42*)

12 July 2013; accepted 4 September 2013
10.1126/science.1243167

Product-to-Parent Reversion of Trenbolone: Unrecognized Risks for Endocrine Disruption

Shen Qu,[1] Edward P. Kolodziej,[2]* Sarah A. Long,[3] James B. Gloer,[3] Eric V. Patterson,[4] Jonas Baltrusaitis,[5,6] Gerrad D. Jones,[2] Peter V. Benchetler,[2] Emily A. Cole,[2] Kaitlin C. Kimbrough,[2] Matthew D. Tarnoff,[1] David M. Cwiertny[1,7]*

Trenbolone acetate (TBA) is a high-value steroidal growth promoter often administered to beef cattle, whose metabolites are potent endocrine-disrupting compounds. We performed laboratory and field phototransformation experiments to assess the fate of TBA metabolites and their photoproducts. Unexpectedly, we observed that the rapid photohydration of TBA metabolites is reversible under conditions representative of those in surface waters (pH 7, 25°C). This product-to-parent reversion mechanism results in diurnal cycling and substantial regeneration of TBA metabolites at rates that are strongly temperature- and pH-dependent. Photoproducts can also react to produce structural analogs of TBA metabolites. These reactions also occur in structurally similar steroids, including human pharmaceuticals, which suggests that predictive fate models and regulatory risk assessment paradigms must account for transformation products of high-risk environmental contaminants such as endocrine-disrupting steroids.

Humans discharge a multitude of bioactive organic contaminants into receiving waters that adversely affect aquatic organisms (*1*–*3*). Risk assessment approaches for regulating these contaminants often are simplistic, typically assuming that if degradation occurs, the associated ecological risk greatly decreases. However, there is growing sentiment that some environmental transformation reactions result in minimal mitigation of risk, forming products that retain bioactive moieties, exhibit greater toxicity, or affect different biological end points (*4*, *5*).

The androgenic steroid trenbolone acetate [TBA; 17β-(acetyloxy)estra-4,9,11-trien-3-one] is an anabolic growth promoter implanted in over 20 million cattle annually (*6*, *7*), with annual revenue attributable to its use likely exceeding $1 billion (*8*). Given the extensive use of TBA, its dominant metabolite [17α-trenbolone (17α-TBOH)] and other known metabolites

[1]Department of Civil and Environmental Engineering, University of Iowa, 4105 Seamans Center for the Engineering Arts and Sciences, Iowa City, IA 52242–1527, USA. [2]Department of Civil and Environmental Engineering, University of Nevada, Reno, Mail Stop 258, Reno, NV 89557, USA. [3]Department of Chemistry, University of Iowa, Iowa City, IA 52242–1527, USA. [4]Department of Chemistry, Truman State University, Kirksville, MO 63501, USA [5]PhotoCatalytic Synthesis Group, MESA+ Institute for Nanotechnology, Faculty of Science and Technology, University of Twente, Meander 225, Post Office Box 217, 7500 AE Enschede, Netherlands. [6]Department of Occupational and Environmental Health, College of Public Health, University of Iowa, Iowa City, IA 52242, USA. [7]Department of Chemical and Biochemical Engineering, University of Iowa, 4133 Seamans Center for the Engineering Arts and Sciences, Iowa City, IA 52242–1527, USA.

*Corresponding author. E-mail: koloj@unr.edu (E.P.K.); david-cwiertny@uiowa.edu (D.M.C.)